Nano Research
2023, 16(7): 8729–8736

ISSN 1998-0124 CN 11-5974/O4
https://doi.org/10.1007/s12274-023-5513-5

Communication

Isolated Cu-Sn diatomic sites for enhanced electroreduction of CO_2 to CO

Wei Liu[1,3,§], Haoqiang Li[4,§], Pengfei Ou[5,§], Jing Mao[6], Lili Han[1,2] (✉), Jun Song[5], Jun Luo[4], and Huolin L. Xin[2] (✉)

[1] *State Key Laboratory of Structural Chemistry, Fujian Institute of Research on the Structure of Matter, Chinese Academy of Sciences, Fuzhou 350002, China*
[2] *Department of Physics and Astronomy, University of California, Irvine, CA 92697, USA*
[3] *Tsinghua Shenzhen International Graduate School, Tsinghua University, Shenzhen 518055, China*
[4] *School of Materials Science and Engineering, Tianjin Key Lab of Photoelectric Materials & Devices, Tianjin University of Technology, Tianjin 300384, China*
[5] *Department of Mining and Materials Engineering, McGill University, Montreal H3A 0C5, Canada*
[6] *Teaching and Analytical Instrumentation Center, School of Materials Science and Engineering, Tianjin University, Tianjin 300072, China*
[§] *Wei Liu, Haoqiang Li, and Pengfei Ou contributed equally to this work.*

Received: 24 October 2022 / **Revised:** 5 January 2023 / **Accepted:** 17 January 2023

ABSTRACT

Electrochemical CO_2 reduction reaction (CO_2RR) to high-value product, CO, not only provides a key feedstock for the well-established Fischer–Tropsch process but also mitigates the greenhouse effect. However, it suffers from sluggish reaction kinetics, competitive hydrogen evolution reaction, and low selectivity. Herein, we report non-precious Cu-Sn diatomic sites anchored on nitrogen-doped porous carbon (CuSn/NPC) as an efficient catalyst for CO_2RR to CO. The catalyst exhibits outstanding selectivity with CO Faradaic efficiency (FE) up to 99.1%, much higher than those of individual Cu (66.2%) and Sn (51.3%) single-atom catalysts. Moreover, high stability is confirmed by consecutive 24 h electrolysis with high selectivity from CO_2 to CO. Theoretical calculations reveal an obvious activation of CO_2 with weakened C–O bonds and distorted CO_2 configuration upon chemisorption on the CuSn/NPC catalyst. It is also suggested CuSn/NPC is more selective for the CO_2RR with dominant CO production during the electrolysis, rather than the competing hydrogen evolution reaction.

KEYWORDS

CO_2 reduction reaction, Cu-Sn active site, CO product, dual-atom electrocatalyst, density functional theory (DFT) calculation

1 Introduction

With the continuous development of human society, energy demand has increased dramatically, and excessive consumption of fossil fuels has caused a worse energy crisis and greenhouse effect [1, 2]. Electrocatalytic CO_2 reduction reaction (CO_2RR) to valuable chemicals is an effective method to solve this status quo [3, 4]. As the primary product of CO_2RR, carbon monoxide (CO) not only can be separated from the electrolyte but also is a key crude material for many essential synthetic hydrocarbons by the mature Fischer–Tropsch process [5–7]. However, some issues remain in CO_2RR to CO, such as sluggish reaction kinetics and competing hydrogen evolution reaction (HER) [8–11]. Therefore, it is important to develop catalysts that boost CO_2RR to CO efficiently. Existing noble metal electrocatalysts (such as Au, Pd, and Ag) have shown excellent performance for CO_2RR to CO at relatively low overpotential [12–14]. However, their scarcity limits their implementation at an industrial scale.

The Cu-based catalyst with the effectiveness of cost and dominant applications in CO_2RR is one of the most promising catalysts for CO_2RR to CO [15–20]. Whereas its low selectivity hinders its development and practical applications in CO_2RR to favorable CO production. To get out of such a predicament, multiple methods for catalyst modification have been developed, such as reducing catalyst size [21–23], introducing another element into one catalyst [24–26], tuning the morphology of catalysts [27–29], and adjusting the surface structure of catalysts [30]. Among them, the size reduction of catalysts to the atomic level has unique advantages of highly efficient atomic utilization, high unsaturated coordination, low metal content, and strong metal–support interaction [31], which renders it become one of the most promising methods [32, 33]. Moreover, recent reports have found that two or more metal atoms close to each other could better cooperate to complete the catalytic reaction compared to individual ones [31, 34–36]. For instance, coupling Cu-based nanoparticles with Sn can change the electronic structure of Cu to improve the Faradaic efficiency (FE) of CO by generating a surface that inhibits the adsorption of H^* and decreases competitive H_2 production [15, 17, 37].

Inspired by the breakthroughs above, we introduce Sn into isolated Cu sites and build isolated Cu-Sn diatomic sites supported on nitrogen-doped three-dimensional porous carbon (CuSn/NPC) for CO_2RR. The introduction of Sn improves FE of CO from 66.2% to 99.1% at −0.75 V vs. reversible hydrogen electrode

Address correspondence to Lili Han, llhan@fjirsm.ac.cn; Huolin L. Xin, huolin.xin@uci.edu

(RHE), all potentials in this work are given vs. RHE unless stated otherwise) and outstanding electrochemical stability during consecutive electrolysis in 0.1 M $KHCO_3$ for 24 h. Of note, the performance of CuSn/NPC is among the best reported for Cu- and Sn-based electrocatalysts (see Table S1 in the Electronic Supplementary Material (ESM)). The density functional theory (DFT) studies reveal that the enhanced performance is attributed to the unique bidentate configuration of Cu-Sn sites, which is conducive to the activation of CO_2 upon chemisorption on CuSn/NPC.

2 Experimental

2.1 Synthesis

Nafion (5 wt.%) was purchased from Sigma-Aldrich. Other chemical reagents were purchased from Sinopharm Chemical Reagent Co., Ltd. All of the reagents were of analytical grade and used without further purification. Deionized water (18 MΩ·cm) was used throughout all experiments.

2.2 Synthesis of CuSn/NPC

In a typical procedure, 1.47 mg cupric chloride ($CuCl_2$), 3.84 mg stannic chloride pentahydrate ($SnCl_4{\cdot}5H_2O$), and 144 mg glucose ($C_6H_{12}O_6$) were ultrasonically dissolved in 40 mL deionized water. 690 mg hydroxylamine hydrochloride ($(NH_3OH)Cl$) was dissolved in 40 mL ethanol. Afterward, the ethanol and the water solutions were mixed. The mixture was stirred for 3 h and dried at 70 °C for 24 h. Subsequently, the dried sample was placed in a porcelain boat, heated from room temperature to 950 °C with a heating rate of 5 °C·min^{-1} under Ar atmosphere protection, and kept for 3 h. After the temperature was cooled down to room temperature, the obtained product was milled into a fine powder and denoted as CuSn/NPC.

2.3 Synthesis of Cu/NPC, Sn/NPC, and NPC

The Cu/NPC was synthesized through the same synthetic procedures as those of CuSn/NPC, except for 2.95 mg $CuCl_2$ instead of 1.47 mg $CuCl_2$ and 3.84 mg $SnCl_4{\cdot}5H_2O$ was added to keep mole numbers of Cu in Cu/NPC the same as that of total Cu and Sn in CuSn/NPC. The Sn/NPC was synthesized through the same synthetic procedures as those of CuSn/NPC except for 7.6 mg $SnCl_4{\cdot}H_2O$ instead of 1.47 mg $CuCl_2$ and 3.84 mg $SnCl_4{\cdot}5H_2O$ was added to keep mole numbers of Sn in Sn/NPC the same as that of total Cu and Sn in CuSn/NPC. The NPC was synthesized through the same synthetic procedures as those of CuSn/NPC except for no $CuCl_2$ and $SnCl_4{\cdot}5H_2O$ were added.

2.4 Characterizations

X-ray diffraction (XRD) measurements were conducted using an X-ray diffractometer (Rigaku D/max 2500) at a scan rate of 15°·min^{-1} in the 2θ range of 10°–90°. Scanning electron microscopy (SEM) images were taken on a Verios 460L operated at 20 kV. Transmission electron microscopy (TEM) images and selected area electron diffraction (SAED) patterns were acquired on an FEI Talos F200X TEM operated at 200 kV. High-angle annular dark-field scanning transmission electron microscopy (HAADF-STEM) images and energy-dispersive X-ray spectroscopy (EDS) mapping were acquired on an FEI Titan Themis Cubed G2 60-300 operated at 200 kV. Nitrogen adsorption/desorption was investigated by an Autosorb-iQ-MP system at 77 K, and specific surface areas of the catalysts were determined by the Brunauer–Emmett–Teller (BET) equation. Inductively coupled plasma-atomic emission spectroscopy (ICP-MS) was used to determine the concentration of Cu and Sn species in products. Raman spectra were recorded on a Horiba evolution in a Raman microscope with a Neon laser at the excitation wavelength of 585 nm. X-ray absorption fine structure (XAFS) measurements of the Cu and Sn K-edge were carried out at beamline TPS 44A of the National Synchrotron Radiation Research Center. X-ray photoelectron spectroscopy (XPS) data were collected on a Kratos AXIS Ultra DLD system with a monochromatic Al Kα radiation as the X-ray source and the internal standard of binding energies was referred to the C 1s peak at 284.8 eV. CO_2 temperature programmed desorption (TPD) (AutoChem1 II 2920) measurements were carried out by using a chemical gas adsorption analyzer.

2.5 Cathode preparation process

Electrode preparation. 6 mg of the catalyst and 500 μL of 5% Nafion perfluorinated resin solution were dispersed in 500 μL of ethanol by ultrasound for 1 h, forming a catalyst ink. Thereafter, the ink was dropped onto a carbon paper with a size of 1 cm × 1 cm, leading to the catalyst loading of 0.5 mg·cm^{-2}. Then, carbon paper was dried overnight in the air at room temperature before electrochemical testing.

2.6 Electrochemical measurements

CO_2 electrolysis. Electrocatalytic CO_2RR measurements were carried out in a three-electrode electrochemical H-cell separated by Nafion 117 membrane in a CO_2-saturated 0.1 M $KHCO_3$ electrolyte (pH = 6.8). The Ag/AgCl and Pt foil were used as the reference electrode and the counter electrode, respectively. The working and reference electrodes were placed in the cathode chamber, while the counter electrode was placed in the anode chamber. The potential was measured on the electrochemical workstation (CHI 660D). All potentials in this study were measured against the Ag/AgCl reference electrode and converted to the RHE reference scale using $E_{RHE} = E_{Ag/AgCl} + 0.197 + 0.0591 \times$ pH with iR compensation.

The high-purity CO_2 was flowed into the cathode chamber for 1 h with a flow rate of 20 mL·min^{-1} until a saturated CO_2 condition was reached, which ensures oxygen gas was removed from the electrolyte before electrolysis. The linear sweep voltammetry (LSV) curves were recorded with a scan rate of 10 mV·s^{-1}. The chronoamperometry tests were performed for 1 h at each potential to collect products. The gas-phase products from the cathode compartment were analyzed by gas chromatography (GC, GC-7890B, Agilent) equipped with a thermal conductivity detector (TCD) and a mechanizer-assisted flame ionization detector (FID). High-purity helium (99.9999%) was used as the carrier gas for the chromatography. The liquid products were analyzed with an AVANCE III HD 400MHz Digital nuclear magnetic resonance (NMR) Spectroscopy using dimethyl sulphoxide (DMSO) as an internal standard.

The calculation of FE for gas products was performed using the following equation

$$FE_{gas}(\%) = (2n \times F)/Q = (2C_{gas} \times V_{CO_2} \times 10^{-3} \times t \times F)/24.8Q \quad (1)$$

where n is the mole amount of gas generated; F is the Faraday constant (96,485 C·mol^{-1}); Q is the total electric charge; C_{gas} is the volume concentration of the gas-phase products, based on the calibration of the GC results; V_{CO_2} is the flow rate of CO_2 (20 mL·min^{-1}); t is electrolysis time (60 min).

The calculation of the yield rate for gas products was performed using the following equation

$$\text{Yield rate} = C_{gas} \times V_{CO_2} \times t/22.4\text{DWT} \quad (2)$$

where DWT is the sample content per unit area.

The partial current density of CO (j_{CO}) was calculated according to

$$j_{CO} = j_{total} \times FE_{CO} \quad (3)$$

where j_{total} is the total current density on the electrode.

2.7 *In situ* fourier transform infrared spectrometer (FTIR)

The *in situ* FTIR measurements were performed on Nicolet 6700 spectrometers (Thermo Fisher, USA) in a region of 500–4000 cm^{-1} with a reflection window integrated with three-electrode cells. A Pt mesh and saturated Ag/AgCl were used as the counter electrode and reference electrode, respectively. 12 μL of catalyst ink was drop-casted onto a glassy carbon electrode (GCE, 3.00 mm in diameter) and was used as the working electrode. 0.1 M $KHCO_3$ electrolyte was constantly purged with high-purity CO_2 gas (20 mL·min^{-1}) during the reaction. The *in situ* electrochemical FTIR spectra were acquired during the chronoamperometry measurements from −0.25 to −1.05 V vs. RHE, and the background spectrum was collected without applied potential. The time-dependent FTIR experiments were performed at −0.75 V by gradually changing the duration of the *i*–*t* test and conducting an infrared test after each *i*–*t* test.

2.8 DFT calculations

All calculations were based on the *ab initio* DFT calculations using projector-augmented wave (PAW) method [38, 39] as implemented in the Vienna *ab initio* simulation package (VASP) code [40] by considering the spin-polarization. The electron exchange-correlation term was described by generalized gradient approximation (GGA) in the parametrization of Perdew–Burke–Ernzerhof (PBE) functional [41] combining with van der Waals correlation derived from the DFT-D2 method of Grimme correlation functional [42]. Cut-off energy of 450 eV was chosen, and structural optimization was achieved until the residual force of each ion was smaller than 0.01 eV·$Å^{-1}$. The convergence criterion for the electronic structure was set to 10^{-5} eV per atom. The electronic structure calculations employed a Fermi-level smearing width, taken as 0.05 eV for all adsorbed species, whereas 0.01 eV for all non-adsorbed species.

To determine the Gibbs free energy change of CO_2RR and HER on various catalytic sites, *ab initio* DFT calculations were performed on the CuN_2SnN_2, CuN_3, and SnN_3 centers residing in a graphene nanoribbon along the zigzag direction with C atoms at the edges passivated with H atoms, denoted as CuN_2SnN_2/Gr, CuN_3/Gr, and SnN_3/Gr respectively. The CuN_3 and SnN_3 centers were chosen herein to guarantee the same coordination numbers as those of Cu and Sn atoms in the CuN_2SnN_2/Gr center. The graphene nanoribbon was duplicated 7 times along the *x*-axis (zigzag) and 5 times along the *y*-axis (armchair), and the two bottommost units were fixed during the structural optimization. All integrations over the Brillouin zone were performed using gamma-centered 2 × 1 × 1 *k*-points.

3 Results and discussion

3.1 Synthesis and characterization

CuSn/NPC was synthesized via a dissolution-and-carbonization method. The obtained product was characterized with SEM and TEM. Figure 1(a) and Fig. S1(a) in the ESM show that CuSn/NPC has a three-dimensional nanoporous structure. This structure was formed due to a large amount of CO_2 and NH_3 gases generated from the decomposition of hydroxylamine hydrochloride and glucose at high temperatures during the carbonization process. The porous structure is conducive to exposure of active sites and improves the mass transport of electrolytes in the process of CO_2RR [43–45]. The absorption–desorption isotherms and pore size distribution in Fig. S2 in the ESM show that CuSn/NPC has a high specific surface area of 274.421 $m^2 \cdot g^{-1}$ and a high-density mesoporous structure with a pore size centered at 3.19 nm. The high-resolution TEM (HRTEM) image in Fig. 1(b) and the SAED pattern in Fig. S1(b) in the ESM demonstrate the amorphousness of CuSn/NPC, which is further confirmed by the X-ray diffraction analysis in Fig. S1(c) in the ESM [46].

The aberration-corrected HAADF-STEM image shows dense atomically dispersed bright dots dispersed on the matrix (Fig. 1(c)). When zooming in on the image, we can find that many bright dots with different contrasts caused by the difference between atomic numbers of Sn and Cu are paired as tagged by the orange circles in Fig. 1(d). The statistical analysis of 50 pairs of the dual atoms in Fig. 1(e) demonstrates an average distance of 0.22 ± 0.04 nm between Cu and Sn as EDS mapping of CuSn/NPC in Fig. 1(f) and Figs. S1(d)–S1(f) in the ESM displays homogeneously distributed Cu, Sn, N, and C elements over the matrix, indicating no aggregation in the sample. Inductively coupled plasma-atomic emission spectroscopy (ICP-AES) reveals the weight percentages of Cu and Sn as 1.21 wt.% and 1.13 wt.%, respectively. In addition, the Raman spectra in Fig. S3 in the ESM show that there are two peaks located at 1340 (D band) and 1560 cm^{-1} (G band), which are ascribed to defects and graphite of carbon, respectively [47]. The intensity ratio of D and G bands (I_D/I_G) of CuSn/NPC is higher than that of Cu/NPC, Sn/NPC, and NPC, indicating that there are more defects in CuSn/NPC.

Figure 2(a) shows that the Cu K-edge X-ray absorption near edge structure (XANES) edge of CuSn/NPC lies between those of Cu_2O and CuO, indicating that the Cu average valence is between +1 and +2, which is identical to the XPS fitting result in Fig. S4(a) in the ESM [46, 48]. Figure 2(b) shows that the Sn XANES edge of CuSn/NPC lies between those of Sn foil and $SnCl_4$, close to that of SnO_2, suggesting that the valence state of Sn in CuSn/NPC is the same as that in SnO_2 (+4), which is further confirmed by the XPS result in Fig. S4 in the ESM [49, 50]. The Cu *R*-space fourier transformed-extended X-ray absorption fine structure (FT-EXAFS) spectra (Fig. 2(c)) and wavelet transform (WT) EXAFS plot (Fig. S5(a) in the ESM) display that the main peak is located at 1.55 Å [51–53], which is assigned to the Cu–N coordination [40]. The Sn *R*-space FT-EXAFS spectra (Fig. 2(d)) and WT-EXAFS plot (Fig. S5(b) in the ESM) present that the main peak is located at 1.49 Å, which is contributed by the coordination of Sn to N [54, 55]. The fitting results of the Cu and Sn at *k*, *q*, and *R* space FT-EXAFS spectra (Figs. 2(c) and 2(d), Fig. S6 and Table S2 in the ESM) and the analyses of the Cu and Sn XPS spectra [56] (Figs. 2(e) and 2(f) and Fig. S4 in the ESM) demonstrate the CuN_2SnN_2 structure in CuSn/NPC, which is consistent with the analysis result from the aberration-corrected HAADF-STEM image in Fig. 1(d).

XPS was utilized to explore the electronic structure of CuSn/NPC and control samples (Cu/NPC and Sn/NPC). The control samples were synthesized via similar approaches for CuSn/NPC (see Section 2.3 for more details). They are composed of atomically dispersed Cu and Sn on N-doped porous carbon, respectively (Figs. S7 and S8 in the ESM). Figure 2(e) displays that Cu $2p_{3/2}$ binding energy of CuSn/NPC shifts to a higher energy direction by 0.5 eV compared with that of Cu/NPC, and Sn $3d_{5/2}$ binding energy of CuSn/NPC shifts to a higher energy direction by 0.3 eV compared with that of Sn/NPC as displayed in Fig. 2(f). By contrast, the C 1s peak of CuSn/NPC has no shift compared with those of Cu/NPC and Sn/NPC (Fig. S9 in the ESM). These

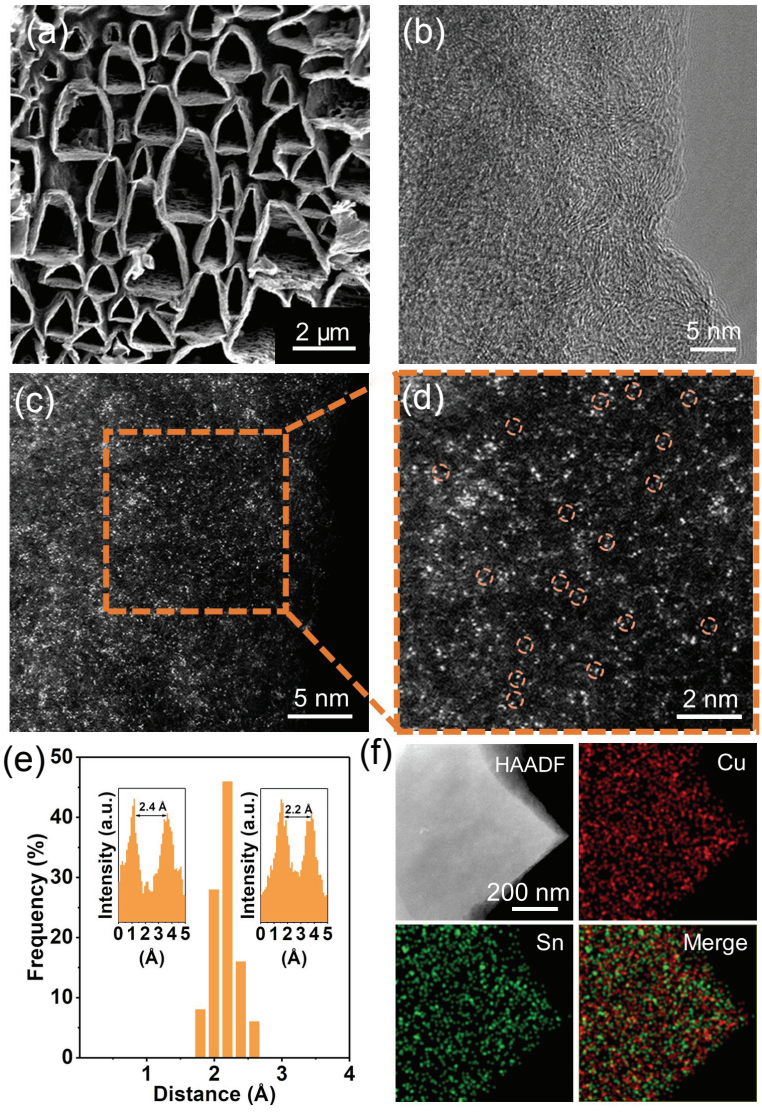

Figure 1 Structural characterizations of CuSn/NPC. (a) Low-magnification SEM image. (b) HRTEM image. (c) Atomic-resolution HAADF-STEM image. (d) Magnified atomic-resolution HAADF-STEM image of the orange frame area in (c). Some atomic pairs are highlighted with orange circles. (e) Statistical Cu–Sn distances in the observed diatomic pairs, in which the two insets are intensity profiles obtained on two bimetallic Cu-Sn sites. (f) HAADF-STEM image and corresponding EDS mapping images of Cu, Sn, and their merge.

comparisons demonstrate electronic interactions between Cu and Sn atoms in CuSn/NPC, suggesting that the introduction of Sn causes the electronic structure change of Cu atoms.

3.2 CO_2RR performances

Electrochemical CO_2RR performances of CuSn/NPC, Cu/NPC, Sn/NPC, and NPC catalysts were evaluated using a three-electrode sealed and Nafion-117 proton exchange membrane-separated H-type cell. The LSV curves in Fig. 3(a) demonstrate that CuSn/NPC has the highest total current density among the four catalysts at applied potentials from −0.4 to −1.0 V. Moreover, the LSV curve of CuSn/NPC in CO_2-saturated $KHCO_3$ electrolyte displays a much larger current density than that obtained in the Ar-saturated $KHCO_3$ electrolyte (Fig. S10 in the ESM), indicating the high CO_2RR activity of CuSn/NPC. The gas and liquid products were analyzed with GC and NMR spectroscopy, respectively. The FE of CuSn/NPC achieves a maximum FE_{CO} of 99.1% at −0.75 V, much higher than those of Cu/NPC (66.2%), Sn/NPC (51.3%), and NPC (7.1%) (Fig. 3(b) and Figs. S11 and S12 in the ESM). Figure 3(c) shows that the CuSn/NPC sample reaches a maximum CO yield rate of 15.45 $mmol \cdot h^{-1} \cdot mg_{cat}^{-1}$ at −0.85 V, which is much higher than those of Cu/NPC (7.14 $mmol \cdot h^{-1} \cdot mg_{cat.}^{-1}$), Sn/NPC (5.96 $mmol \cdot h^{-1} \cdot mg_{cat}^{-1}$), and NPC (0.21 $mmol \cdot h^{-1} \cdot mg_{cat}^{-1}$). Figure 3(d) discloses that the current density of CuSn/NPC increases sharply with the increase of the applied potential and reaches 10.22 $mA \cdot cm^{-2}$ at −0.95 V, much higher than the other three catalysts at the same potential. To shed light on the reaction kinetics of the catalysts, we plotted and analyzed their Tafel slopes. As shown in Fig. 3(e), CuSn/NPC achieves a Tafel slope of 142 $mV \cdot dec^{-1}$, smaller than those of Cu/NPC (178 $mV \cdot dec^{-1}$) and Sn/NPC (196 $mV \cdot dec^{-1}$), indicating the lowest activation energy barrier and the fastest reaction kinetics during the CO_2RR.

To unravel the fundamental cause of the enhanced CO_2 electroreduction performances, we performed CO_2-TPD and *in situ* FTIR measurements. Figure S13 in the ESM shows a much larger CO_2 desorption area in the CuSn/NPC relative to Cu/NPC and Sn/NPC, which demonstrates that the CuSn/NPC has a larger capability of CO_2 adsorption [57, 58]. The electrochemical *in situ* FTIR spectra in Fig. S14(a) in the ESM show that an obvious downward peak emerges at 1400 cm^{-1} with the potential decreases to −0.25 V, which is assigned to the C–O stretching of *COOH intermediate [59, 60]. The intensity of the *COOH band gradually increases and then achieves the maximum at −0.75 V, which is in agreement with the above CO_2RR performances. Figure S14(b) in the ESM shows that the intensity of the *COOH band gradually

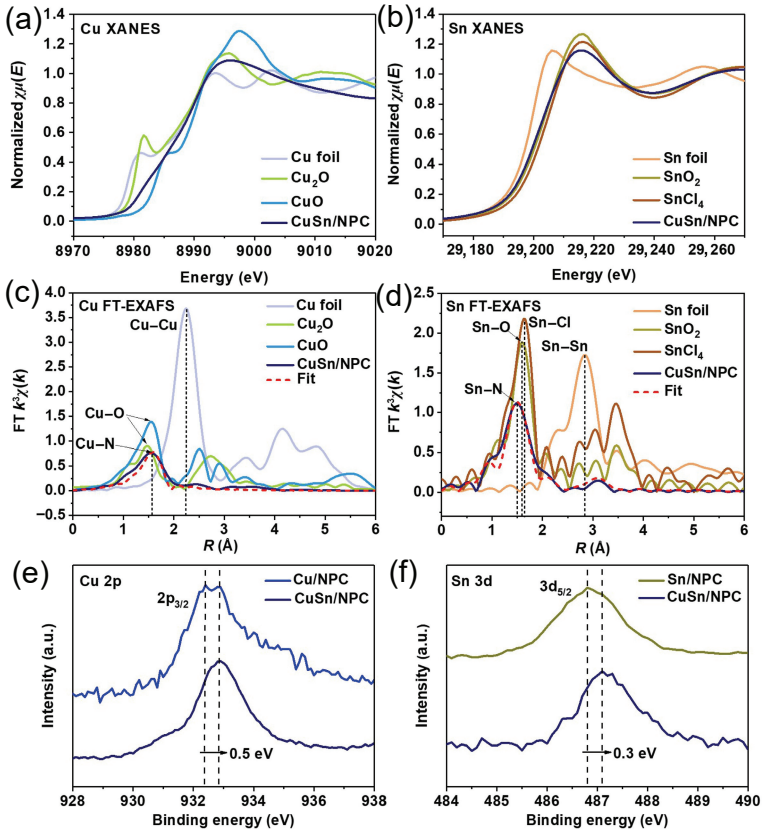

Figure 2 Synchrotron radiation XAFS and XPS measurements. (a) Cu K-edge XANES spectra of CuSn/NPC and reference samples (Cu foil, Cu_2O, and CuO). (b) Sn K-edge XANES spectra of CuSn/NPC and reference samples (Sn foil, $SnCl_4$, and SnO_2). (c) Cu K-edge and (d) Sn K-edge FT-EXAFS spectra of CuSn/NPC and their reference samples. (e) Cu 2p XPS spectra of CuSn/NPC and Cu/NPC. (f) Sn 3d XPS spectra of CuSn/NPC and Sn/NPC.

increases with reaction time, achieving the maximum at 270 s, and then reaches a dynamic balance. The *in situ* FTIR experiments verify the formation of *COOH intermediate during the CO_2RR.

Moreover, electrocatalytic stability is an important measure of CO_2RR performance. Figure 3(f) displays that the total current density value remains nearly unchanged, and FE_{CO} maintains over 96% during continuous 24 h electrolysis at −0.75 V. The characterizations of CuSn/NPC after long-term CO_2RR electrolysis demonstrate that the morphology and element distribution are retained (Fig. S15 in the ESM). Similarly, the valence states of Cu and Sn in CuSn/NPC after CO_2RR electrolysis are verified to be consistent with those of the pristine CuSn/NPC before electrolysis (Fig. S16 in the ESM). These findings confirm the robustness of CuSn/NPC during CO_2RR.

3.3 DFT studies

To further understand the mechanism of the enhanced CO_2RR activity, we first examined the CO_2 adsorption and activation using DFT calculations since the initial activation of the inert CO_2 is the prerequisite for an efficient CO_2RR process. Illustrated in Figs. 4(a)–4(c) are the comparisons between different degrees of CO_2 activation on CuN_2SnN_2/Gr, CuN_3/Gr, and SnN_3/Gr, respectively (see Section 2.8 for more details). For CO_2* adsorption on CuN_2SnN_2/Gr (Fig. 4(a)), the C atom strongly binds to the Cu atom with a bond length of 1.98 Å, and one O atom attaches to the Sn atom with a longer bond length of 2.36 Å, with an adsorption energy of 0.42 eV. A bidentate configuration is therefore formed, facilitating the subsequent reactions, resulting in a significant distortion of CO_2 from its original linear form to a bent form with an O–C–O angle of 133.03°. In addition, the interaction between CO_2 and CuN_2SnN_2/G weakens the two C–O bonds of CO_2, leading to elongated C–O bonds (1.28 and 1.23 Å) from the original bond length of 1.18 Å for an isolated CO_2. On the other hand, CO_2 attached on CuN_3/Gr with a longer bond length of 2.12 Å between C and Cu, a larger O–C–O angle of 149.64° (Fig. 4(b)), if compared with those of CuN_2SnN_2/Gr. Besides, CO_2 fails to chemically adsorb on SnN_3/Gr and remains in the original linear configuration with the O–C–O angle of 179.89°, with two C–O bond lengths similar to those in the isolated gas phase (Fig. 4(c)). Collectively, the weakened C–O bonds and the distorted CO_2 configuration together highlight an obvious activation of CO_2 upon chemisorption at CuN_2SnN_2/Gr, which is in contrast to the negligible activation of CO_2 on CuN_3/Gr and SnN_3/Gr (adsorption energy of 0.54 and 0.60 eV, respectively). Due to the CO_2 activation achieved on the CuN_2SnN_2/G (Fig. 4(d)), the COOH* formation is an exothermic process with the Gibbs free energy change (ΔG) of −0.56 eV with the potential-determining step (PDS) being the transformation of COOH* to CO* (ΔG = 0.36 eV). Meanwhile, the COOH* formation is the PDS for CO_2RR on CuN_3/Gr and SnN_3/Gr with ΔG of 0.72 and 1.34 eV respectively, and the relatively large ΔG results in an inactive CO_2RR process.

Further, we also estimated the selectivity between CO_2RR and HER on these catalytic sites, since HER is the major competing reaction in the electrochemical environment. In general, from a theoretical perspective, the selectivity between CO_2RR and HER is given by the difference between the limiting potentials, i.e., $\Delta U_L = U_L(CO_2RR) - U_L(HER)$ (Fig. S17 in the ESM). A more negative value suggests a catalyst more selective to HER, whereas a more positive value indicates more selective to CO_2RR. As shown in Fig. 4(e), CuN_2SnN_2/Gr shows the most positive ΔU_L value demonstrating that it will selectively produce CO during the electrolysis. However, CuN_3/Gr and SnN_3/Gr with a negative ΔU_L value are expected to interact more selectively with protons to generate H_2. We note that the high selectivity achieved on CuN_2SnN_2/Gr towards the CO_2-to-CO generation also results

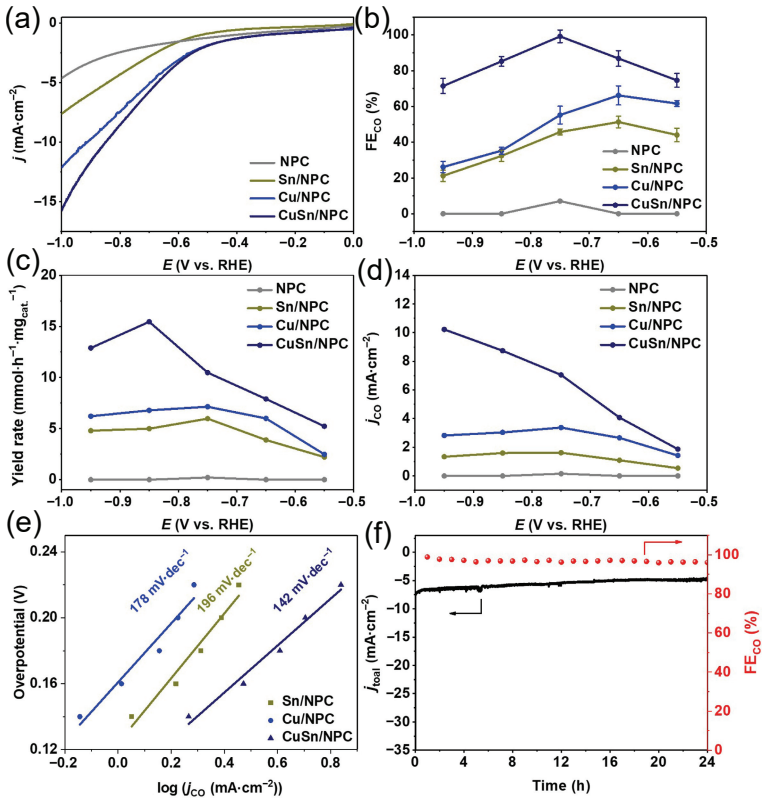

Figure 3 CO_2RR performance of CuSn/NPC. (a) LSV curves obtained in CO_2-saturated 0.1 M $KHCO_3$ electrolyte. (b) FE_{CO}, (c) CO yield rates, and (d) j_{CO} of CuSn/NPC, Cu/NPC, Sn/NPC, and NPC at various applied potentials. (e) Tafel plots of CuSn/NPC, Cu/NPC, and Sn/NPC. (f) Total current density and FEs stability test for CuSn/NPC during 24 h electrolysis at −0.75 V.

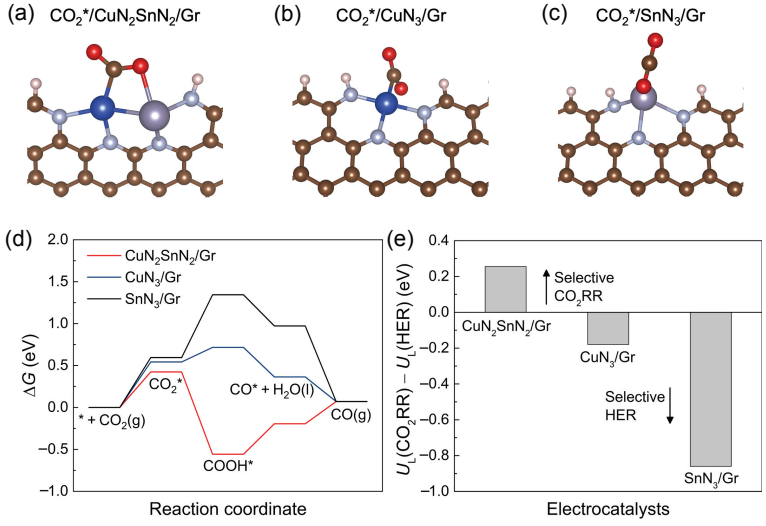

Figure 4 CO_2RR activity and selectivity from DFT calculations. Comparisons among different degrees of CO_2 activation and adsorption on (a) CuN_2SnN_2/Gr, (b) CuN_3/Gr, and (c) SnN_3/Gr, respectively (blue: copper; dark silver: tin; light sliver: nitrogen; red: oxygen; brown: carbon; pink: hydrogen). (d) ΔG diagram for CO_2RR and (e) selectivity between CO_2RR and HER ($U_L(CO_2RR) - U_L(HER)$) on CuN_2SnN_2/Gr, CuN_3/Gr, and SnN_3/Gr, respectively.

from the fact that the HCOOH pathway is prohibited by a large uphill energy for the hydrogenation of HCOO* to HCOOH (Fig. S18 in the ESM).

4 Conclusions

In summary, Cu-Sn diatomic sites anchored on N-doped porous carbon are demonstrated to serve as an efficient and selective electrocatalyst for CO_2RR to CO. The aberration-corrected HAADF-STEM and XAFS results identify the structure of the Cu-Sn diatomic sites. The high selectivity of CO_2RR to CO and outstanding FEs stability during consecutive 24 h electrolysis make CuSn/NPC one of the top-class catalysts among the Cu- and Sn-based electrocatalysts ever reported. DFT calculations reveal that the weakened C–O bonds and the distorted CO_2 configuration together highlight an obvious activation of CO_2 upon chemisorption and selective CO generation during the electrolysis at CuN_2SnN_2/Gr. This work paves a prospective way to design electrocatalysts with diatomic sites for CO_2RR.

Acknowledgements

This work was supported by the startup funding of H. L. X. The XAFS/EXAFS spectra obtained from beamline TPS 44A at National Synchrotron Radiation Research Center (NSRRC) are appreciated. The authors thank Hsiao-Tsu Wang, Wei-Xuan Lin, Chih-Wen Pao, and Way-Faung Pong for the acquisition and analysis of the XAFS data.

Electronic Supplementary Material: Supplementary material (supplementary TEM, STEM, XRD, BET, Raman, XPS, EXAFS, NMR, TPD, and FTIR characterizations, electrocatalytic measurements, and DFT calculations) is available in the online version of this article at https://doi.org/10.1007/s12274-023-5513-5.

References

[1] Chu, S.; Majumdar, A. Opportunities and challenges for a sustainable energy future. *Nature* **2012**, *488*, 294–303.

[2] Davis, S. J.; Caldeira, K.; Matthews, H. D. Future CO_2 emissions and climate change from existing energy infrastructure. *Science* **2010**, *329*, 1330–1333.

[3] Han, L. L.; Song, S. J.; Liu, M. J.; Yao, S. Y.; Liang, Z. X.; Cheng, H.; Ren, Z. H.; Liu, W.; Lin, R. Q.; Qi, G. C. et al. Stable and efficient single-atom Zn catalyst for CO_2 reduction to CH_4. *J. Am. Chem. Soc.* **2020**, *142*, 12563–12567.

[4] Kauffman, D. R.; Thakkar, J.; Siva, R.; Matranga, C.; Ohodnicki, P. R.; Zeng, C. J.; Jin, R. C. Efficient electrochemical CO_2 conversion powered by renewable energy. *ACS Appl. Mater. Interfaces* **2015**, *7*, 15626–15632.

[5] Rofer-DePoorter, C. K. A comprehensive mechanism for the Fischer–Tropsch synthesis. *Chem. Rev.* **1981**, *81*, 447–474.

[6] Vennestrøm, P. N. R.; Osmundsen, C. M.; Christensen, C. H.; Taarning, E. Beyond petrochemicals: The renewable chemicals industry. *Angew. Chem., Int. Ed.* **2011**, *50*, 10502–10509.

[7] Zhang, Y. Q.; Jacobs, G.; Sparks, D. E.; Dry, M. E.; Davis, B. H. CO and CO_2 hydrogenation study on supported cobalt Fischer–Tropsch synthesis catalysts. *Catal. Today* **2022**, *71*, 411–418.

[8] Buckley, A. K.; Lee, M.; Cheng, T.; Kazantsev, R. V.; Larson, D. M.; Goddard Iii, W. A.; Toste, F. D.; Toma, F. M. Electrocatalysis at organic-metal interfaces: Identification of structure–reactivity relationships for CO_2 reduction at modified Cu surfaces. *J. Am. Chem. Soc.* **2019**, *141*, 7355–7364.

[9] Liu, M.; Pang, Y. J.; Zhang, B.; De Luna, P.; Voznyy, O.; Xu, J. X.; Zheng, X. L.; Dinh, C. T.; Fan, F. J.; Cao, C. H. et al. Enhanced electrocatalytic CO_2 reduction via field-induced reagent concentration. *Nature* **2016**, *537*, 382–386.

[10] Rosen, B. A.; Salehi-Khojin, A.; Thorson, M. R.; Zhu, W.; Whipple, D. T.; Kenis, P. J. A.; Masel, R. I. Ionic liquid-mediated selective conversion of CO_2 to CO at low overpotentials. *Science* **2011**, *334*, 643–644.

[11] Jiao, Y.; Zheng, Y.; Chen, P.; Jaroniec, M.; Qiao, S. Z. Molecular scaffolding strategy with synergistic active centers to facilitate electrocatalytic CO_2 reduction to hydrocarbon/alcohol. *J. Am. Chem. Soc.* **2017**, *139*, 18093–18100.

[12] He, Q.; Lee, J. H.; Liu, D. B.; Liu, Y. M.; Lin, Z. X.; Xie, Z. H.; Hwang, S.; Kattel, S.; Song, L.; Chen, J. G. Accelerating CO_2 electroreduction to CO over Pd single-atom catalyst. *Adv. Funct. Mater.* **2020**, *30*, 2000407.

[13] Li, Y. F.; Chen, C.; Cao, R.; Pan, Z. W.; He, H.; Zhou, K. B. Dual-atom Ag_2/graphene catalyst for efficient electroreduction of CO_2 to CO. *Appl. Catal. B:Environ.* **2020**, *268*, 118747.

[14] Li, J.; Chen, W. D.; Lin, R.; Huang, M. R.; Wang, M.; Chai, M. S.; Zhu, H. W. Thermally evaporated Ag-Au bimetallic catalysts for efficient electrochemical CO_2 reduction. *Part. Part. Syst. Charact.* **2021**, *38*, 2100148.

[15] Zhao, Y.; Wang, C. Y.; Wallace, G. G. Tin nanoparticles decorated copper oxide nanowires for selective electrochemical reduction of aqueous CO_2 to CO. *J. Mater. Chem. A* **2016**, *4*, 10710–10718.

[16] Yang, H.; Hu, Y. W.; Chen, J. J.; Balogun, M. S.; Fang, P. P.; Zhang, S. Q.; Chen, J.; Tong, Y. X. Intermediates adsorption engineering of CO_2 electroreduction reaction in highly selective heterostructure Cu-based electrocatalysts for CO production. *Adv. Energy Mater.* **2019**, *9*, 1901396.

[17] Sarfraz, S.; Garcia-Esparza, A. T.; Jedidi, A.; Cavallo, L.; Takanabe, K. Cu-Sn bimetallic catalyst for selective aqueous electroreduction of CO_2 to CO. *ACS Catal.* **2016**, *6*, 2842–2851.

[18] Jiang, X. X.; Wang, X. K.; Liu, Z. J.; Wang, Q. L.; Xiao, X.; Pan, H. P.; Li, M.; Wang, J. W.; Shao, Y.; Peng, Z. Q. et al. A highly selective tin-copper bimetallic electrocatalyst for the electrochemical reduction of aqueous CO_2 to formate. *Appl. Catal. B:Environ.* **2019**, *259*, 118040.

[19] Weng, Z.; Zhang, X.; Wu, Y. S.; Huo, S. J.; Jiang, J. B.; Liu, W.; He, G. J.; Liang, Y. Y.; Wang, H. L. Self-cleaning catalyst electrodes for stabilized CO_2 reduction to hydrocarbons. *Angew. Chem., Int. Ed.* **2017**, *56*, 13135–13139.

[20] Schreier, M.; Héroguel, F.; Steier, L.; Ahmad, S.; Luterbacher, J. S.; Mayer, M. T.; Luo, J. S.; Grätzel, M. Solar conversion of CO_2 to CO using earth-abundant electrocatalysts prepared by atomic layer modification of CuO. *Nat. Energy* **2017**, *2*, 17087.

[21] Jiao, J. Q.; Lin, R.; Liu, S. J.; Cheong, W. C.; Zhang, C.; Chen, Z.; Pan, Y.; Tang, J. G.; Wu, K. L.; Hung, S. F. et al. Copper atom-pair catalyst anchored on alloy nanowires for selective and efficient electrochemical reduction of CO_2. *Nat. Chem.* **2019**, *11*, 222–228.

[22] Reske, R.; Mistry, H.; Behafarid, F.; Roldan Cuenya, B.; Strasser, P. Particle size effects in the catalytic electroreduction of CO_2 on Cu nanoparticles. *J. Am. Chem. Soc.* **2014**, *136*, 6978–6986.

[23] Ma, M.; Djanashvili, K.; Smith, W. A. Controllable hydrocarbon formation from the electrochemical reduction of CO_2 over Cu nanowire arrays. *Angew. Chem., Int. Ed.* **2016**, *55*, 6680–6684.

[24] Watanabe, M.; Shibata, M.; Katoh, A.; Sakata, T.; Azuma, M. Design of alloy electrocatalysts for CO_2 reduction: Improved energy efficiency, selectivity, and reaction rate for the CO_2 electroreduction on Cu alloy electrodes. *J. Electroanal. Chem. Interfacial Electrochem.* **1991**, *305*, 319–328.

[25] Kim, D.; Resasco, J.; Yu, Y.; Asiri, A. M.; Yang, P. D. Synergistic geometric and electronic effects for electrochemical reduction of carbon dioxide using gold-copper bimetallic nanoparticles. *Nat. Commun.* **2014**, *5*, 4948.

[26] Rasul, S.; Anjum, D. H.; Jedidi, A.; Minenkov, Y.; Cavallo, L.; Takanabe, K. A highly selective copper-indium bimetallic electrocatalyst for the electrochemical reduction of aqueous CO_2 to CO. *Angew. Chem., Int. Ed.* **2015**, *54*, 2146–2150.

[27] Zhuang, T. T.; Liang, Z. Q.; Seifitokaldani, A.; Li, Y.; De Luna, P.; Burdyny, T.; Che, F. L.; Meng, F.; Min, Y. M.; Quintero-Bermudez, R. et al. Steering post-C–C coupling selectivity enables high efficiency electroreduction of carbon dioxide to multi-carbon alcohols. *Nat. Catal.* **2018**, *1*, 421–428.

[28] Manthiram, K.; Beberwyck, B. J.; Alivisatos, A. P. Enhanced electrochemical methanation of carbon dioxide with a dispersible nanoscale copper catalyst. *J. Am. Chem. Soc.* **2014**, *136*, 13319–13325.

[29] Roberts, F. S.; Kuhl, K. P.; Nilsson, A. High selectivity for ethylene from carbon dioxide reduction over copper nanocube electrocatalysts. *Angew. Chem., Int. Ed.* **2015**, *54*, 5179–5182.

[30] Verdaguer-Casadevall, A.; Li, C. W.; Johansson, T. P.; Scott, S. B.; McKeown, J. T.; Kumar, M.; Stephens, I. E. L.; Kanan, M. W.; Chorkendorff, I. Probing the active surface sites for CO reduction on oxide-derived copper electrocatalysts. *J. Am. Chem. Soc.* **2015**, *137*, 9808–9811.

[31] Ren, W. H.; Tan, X.; Yang, W. F.; Jia, C.; Xu, S. M.; Wang, K. X.; Smith, S. C.; Zhao, C. Isolated diatomic Ni-Fe metal-nitrogen sites for synergistic electroreduction of CO_2. *Angew. Chem., Int. Ed.* **2019**, *58*, 6972–6976.

[32] Yang, X. F.; Wang, A. Q.; Qiao, B. T.; Li, J. Y.; Liu, J.; Zhang, T. Single-atom catalysts: A new frontier in heterogeneous catalysis. *Acc. Chem. Res.* **2013**, *46*, 1740–1748.

[33] Zhu, C. Z.; Fu, S. F.; Shi, Q. R.; Du, D.; Lin, Y. H. Single-atom electrocatalysts. *Angew. Chem., Int. Ed.* **2017**, *56*, 13944–13960.

[34] Yang, X.; Tat, T.; Libanori, A.; Cheng, J.; Xuan, X. X.; Liu, N.; Yang, X.; Zhou, J. H.; Nashalian, A.; Chen, J. Single-atom catalysts with bimetallic centers for high-performance electrochemical CO_2 reduction. *Mater. Today* **2021**, *45*, 54–61.

[35] Gao, D. F.; Liu, T. F.; Wang, G. X.; Bao, X. H. Structure sensitivity in single-atom catalysis toward CO_2 electroreduction. *ACS Energy Lett.* **2021**, *6*, 713–727.

[36] Yun, R. R.; Zhan, F. Y.; Wang, X. J.; Zhang, B. B.; Sheng, T.; Xin, Z. F.; Mao, J. J.; Liu, S. J.; Zheng, B. S. Design of binary Cu-Fe sites coordinated with nitrogen dispersed in the porous carbon for synergistic CO_2 electroreduction. *Small* **2021**, *17*, 2006951.

[37] Huo, S. J.; Weng, Z.; Wu, Z. S.; Zhong, Y. R.; Wu, Y. S.; Fang, J.

H.; Wang, H. L. Coupled metal/oxide catalysts with tunable product selectivity for electrocatalytic CO_2 reduction. *ACS Appl. Mater. Interfaces* **2017**, *9*, 28519–28526.

[38] Kohn, W.; Sham, L. J. Self-consistent equations including exchange and correlation effects. *Phys. Rev.* **1965**, *140*, A1133–A1138.

[39] Notario-Estévez, A.; Kozlov, S. M.; Viñes, F.; Illas, F. Electronic-structure-based material descriptors: (In) dependence on self-interaction and Hartree–Fock exchange. *Chem. Commun.* **2015**, *51*, 5602–5605.

[40] Kresse, G.; Joubert, D. From ultrasoft pseudopotentials to the projector augmented-wave method. *Phys. Rev. B* **1999**, *59*, 1758–1775.

[41] Perdew, J. P.; Burke, K.; Ernzerhof, M. Generalized gradient approximation made simple. *Phys. Rev. Lett.* **1996**, *77*, 3865–3868.

[42] Grimme, S. Semiempirical GGA-type density functional constructed with a long-range dispersion correction. *J. Comput. Chem.* **2006**, *27*, 1787–1799.

[43] Han, L. L.; Hou, M. C.; Ou, P. F.; Cheng, H.; Ren, Z. H.; Liang, Z. X.; Boscoboinik, J. A.; Hunt, A.; Waluyo, I.; Zhang, S. S. et al. Local modulation of single-atomic Mn sites for enhanced ambient ammonia electrosynthesis. *ACS Catal.* **2021**, *11*, 509–516.

[44] Han, L. L.; Liu, X. J.; Chen, J. P.; Lin, R. Q.; Liu, H. X.; Lü, F.; Bak, S.; Liang, Z. X.; Zhao, S. Z.; Stavitski, E. et al. Atomically dispersed molybdenum catalysts for efficient ambient nitrogen fixation. *Angew. Chem., Int. Ed.* **2019**, *58*, 2321–2325.

[45] Han, L. L.; Ou, P. D.; Liu, W.; Wang, X.; Wang, H. T.; Zhang, R.; Pao, C. W.; Liu, X. J.; Pong, W. F.; Song, J. et al. Design of Ru-Ni diatomic sites for efficient alkaline hydrogen oxidation. *Sci. Adv.* **2022**, *8*, eabm3779.

[46] Han, L. L.; Cheng, H.; Liu, W.; Li, H. Q.; Ou, P. F.; Lin, R. Q.; Wang, H. T.; Pao, C. W.; Head, A. R.; Wang, C. H. et al. A single-atom library for guided monometallic and concentration-complex multimetallic designs. *Nat. Mater.* **2022**, *21*, 681–688.

[47] Liu, W.; Han, L. L.; Wang, H. T.; Zhao, X. R.; Boscoboinik, J. A.; Liu, X. J.; Pao, C. W.; Sun, J. Q.; Zhuo, L. C.; Luo, J. et al. FeMo sub-nanoclusters/single atoms for neutral ammonia electrosynthesis. *Nano Energy* **2020**, *77*, 105078.

[48] Sun, H. Z.; Zelekew, O. A.; Chen, X. Y.; Guo, Y. B.; Kuo, D. H.; Lu, Q. X.; Lin, J. G. A noble bimetal oxysulfide Cu*V*OS catalyst for highly efficient catalytic reduction of 4-nitrophenol and organic dyes. *RSC Adv.* **2019**, *9*, 31828–31839.

[49] Gnana Sundara Raj, B.; Angulakshmi, R.; Baskaran, N.; Wu, J. J.; Anandan, S.; Ashokkumar, M. Pseudocapacitive performance of Mn_3O_4-SnO_2 hybrid nanoparticles synthesized via ultrasonication approach. *J. Appl. Electrochem.* **2020**, *50*, 609–619.

[50] Kang, Y.; Park, J. Y.; Kim, D. W.; Kim, H.; Kang, Y. C. Antibacterial and physicochemical properties of Co-sputtered CuSn thin films. *Surf. Interface Anal.* **2018**, *50*, 138–145.

[51] Chen, D. T.; Zhang, L. H.; Du, J.; Wang, H. H.; Guo, J. Y.; Zhan, J. Y.; Li, F.; Yu, F. S. A tandem strategy for enhancing electrochemical CO_2 reduction activity of single-atom Cu-S_1N_3 catalysts via integration with Cu nanoclusters. *Angew. Chem., Int. Ed.* **2021**, *60*, 24022–24027.

[52] Zhang, T.; Nie, X. W.; Yu, W. W.; Guo, X. W.; Song, C. S.; Si, R.; Liu, Y. F.; Zhao, Z. K. Single atomic Cu-N_2 catalytic sites for highly active and selective hydroxylation of benzene to phenol. *iScience* **2019**, *22*, 97–108.

[53] Wang, G.; Huang, R.; Zhang, J. W.; Mao, J. J.; Wang, D. S.; Li, Y. D. Synergistic modulation of the separation of photo-generated carriers via engineering of dual atomic sites for promoting photocatalytic performance. *Adv. Mater.* **2021**, *33*, 2105904.

[54] Guo, J. Y.; Zhang, W. L.; Zhang, L. H.; Chen, D. T.; Zhan, J. Y.; Wang, X. L.; Shiju, N. R.; Yu, F. S. Control over electrochemical CO_2 reduction selectivity by coordination engineering of tin single-atom catalysts. *Adv. Sci.* **2021**, *8*, 2102884.

[55] Zhang, Y. Z.; Jang, H.; Ge, X.; Zhang, W.; Li, Z. J.; Hou, L. Q.; Zhai, L.; Wei, X. Q.; Wang, Z.; Kim, M. G. et al. Single-atom Sn on tensile-strained ZnO nanosheets for highly efficient conversion of CO_2 into formate. *Adv. Energy Mater.* **2022**, *12*, 2202695.

[56] Bulushev, D. A.; Chuvilin, A. L.; Sobolev, V. I.; Stolyarova, S. G.; Shubin, Y. V.; Asanov, I. P.; Ishchenko, A. V.; Magnani, G.; Riccò, M.; Okotrub, A. V. et al. Copper on carbon materials: Stabilization by nitrogen doping. *J. Mater. Chem. A* **2017**, *5*, 10574–10583.

[57] Zu, X. L.; Li, X. D.; Liu, W.; Sun, Y. F.; Xu, J. Q.; Yao, T.; Yan, W. S.; Gao, S.; Wang, C. M.; Wei, S. Q. et al. Efficient and robust carbon dioxide electroreduction enabled by atomically dispersed $Sn^{\delta+}$ sites. *Adv. Mater.* **2019**, *31*, 1808135.

[58] Henderson, M. A. An HREELS and TPD study of water on TiO_2(110): The extent of molecular versus dissociative adsorption. *Surf. Sci.* **1996**, *355*, 151–166.

[59] Zhong, X. H.; Liang, S. J.; Yang, T. T.; Zeng, G. C.; Zhong, Z. Q.; Deng, H.; Zhang, L.; Sun, X. L. Sn dopants with synergistic oxygen vacancies boost CO_2 electroreduction on CuO nanosheets to CO at low overpotential. *ACS Nano* **2022**, *16*, 19210–19219.

[60] Chi, S. Y.; Chen, Q.; Zhao, S. S.; Si, D. H.; Wu, Q. J.; Huang, Y. B.; Cao, R. Three-dimensional porphyrinic covalent organic frameworks for highly efficient electroreduction of carbon dioxide. *J. Mater. Chem. A* **2022**, *10*, 4653–4659.